OCEANOGRAPHY

Dependence of regional ocean heat uptake on anthropogenic warming scenarios

Xiaofan Ma[1,2,3], Wei Liu[2], Robert J. Allen[2], Gang Huang[1,3,4]*, Xichen Li[5]

The North Atlantic and Southern Ocean exhibit enhanced ocean heat uptake (OHU) during recent decades while their future OHU changes are subject to great uncertainty. Here, we show that regional OHU patterns in these two basins are highly dependent on the trajectories of aerosols and greenhouse gases (GHGs) in future scenarios. During the 21st century, North Atlantic and Southern Ocean OHU exhibit similarly positive trends under a business-as-usual scenario but respectively positive and negative trends under a mitigation scenario. The opposite centurial OHU trends in the Southern Ocean can be attributed partially to distinct GHG trajectories under the two scenarios while the common positive centurial OHU trends in the North Atlantic are mainly due to aerosol effects. Under both scenarios, projected decline of anthropogenic aerosols potentially induces a weakening of the Atlantic Meridional Overturning Circulation and a divergence of meridional oceanic heat transport, which leads to enhanced OHU in the subpolar North Atlantic.

INTRODUCTION

Since the industrial era, Earth's energy imbalance has largely been caused by changes in greenhouse gases (GHGs) and aerosols due to human activities (*1*). Global oceans absorb 93% of the net energy (*1*) through air-sea heat flux or in the form of the so-called ocean heat uptake (OHU). Regional OHU change is of great importance for regional sea level change (*2*), transient climate sensitivity and related feedbacks (*3*, *4*), and meridional displacement of the intertropical convergence zone (*5*, *6*). Throughout the historical period (1850–2005), the broad Southern Ocean has accounted for a majority of global OHU while the North Atlantic has taken a relatively smaller share (*7*–*9*). This asymmetry of OHU and ocean heat distribution could be attributed largely to the concurrent increases in GHGs and aerosols during the past century (*10*–*12*) and also to the alterations of deep ocean circulations in these two basins (*13*–*21*). In the North Atlantic, the warming effect of increasing GHGs leads to a weakening of the Atlantic Meridional Overturning Circulation (AMOC) and an increase of OHU, while the cooling effect of increasing aerosols has opposite influences on the AMOC and OHU (*22*, *23*). As a result of the compensation between the effects of aerosols and GHGs, the North Atlantic has shown a relatively small OHU increase during the historical period. On the other hand, anthropogenic aerosols are mainly confined to the Northern Hemisphere (*24*), which is quite different from GHGs that are homogeneously distributed over the globe. Over the Southern Ocean, increasing GHGs have served as one key factor in determining the intensive deep-water upwellings and enhanced OHU (*19*), whereas aerosols have had minimal impacts in this region.

Future emissions of GHGs and aerosols in the 21st century will be different from those in the historical period, as quantified by the Coupled Model Intercomparison Project Phase 5 (CMIP5) Representative Concentration Pathways (RCPs) (*25*). For example, the RCP8.5 scenario is a business-as-usual scenario while the RCP2.6 scenario is a mitigation scenario close to the target of the 2015 Paris Agreement that limits global warming of 1.5°C above preindustrial levels by 2100 (*26*). Both scenarios feature large and similar reductions in anthropogenic aerosol emissions (e.g., ~80% reduction in SO_2 emission by 2100) (*25*) but include different changes in GHG concentrations. For example, atmospheric CO_2 concentration will peak around 2050 and then decrease under the RCP2.6 scenario but will continue to increase throughout the 21st century under the RCP8.5 scenario (*25*). Such different evolutions of aerosols and GHGs will lead to a large scenario-driven uncertainty in regional OHU, indicating that future regional OHU change under the RCP2.6 scenario could be notably different from that under the RCP8.5 scenario (*12*, *22*, *27*). Nevertheless, the characteristics and underlying mechanisms of this scenario-driven uncertainty in regional OHU remain unclear.

RESULTS

Scenario-driven uncertainty in regional OHU

To explore the scenario-driven uncertainty in regional OHU, we examine CMIP5 RCP2.6 and RCP8.5 simulations. We use the multimodel ensemble mean (MME) of 26 CMIP5 models (table S1 and Materials and Methods) to minimize the effects of internal variability and intermodel uncertainty. We examine the long-term trends (Materials and Methods) of regional OHU during the 21st century under both scenarios (Fig. 1). Under the RCP2.6 scenario, OHU exhibits generally opposite trends between hemispheres: a significant positive trend in the subpolar North Atlantic but a negative trend in the Southern Ocean during 2006–2100 (Fig. 1A). These OHU trend patterns are consistent with the time series of regionally averaged OHU (Fig. 1C). In the subpolar North Atlantic, the averaged OHU increases rapidly before 2050 (0.139 W m^{-2} $year^{-1}$, $P < 0.01$) and levels off or declines slightly after that, which corresponds to a positive trend of 0.045 W m^{-2} $year^{-1}$ ($P < 0.01$) during 2006–2100. On the other hand, in the Southern Ocean, the averaged OHU shows a very weak increase by the late 2030s (0.035 W m^{-2} $year^{-1}$, $P < 0.01$) but a large decrease afterward, which corresponds to a negative trend of −0.017 W m^{-2} $year^{-1}$ ($P < 0.01$) during 2006–2100. Note that Southern Ocean OHU begins to decrease one to two decades earlier

[1]State Key Laboratory of Numerical Modeling for Atmospheric Sciences and Geophysical Fluid Dynamics, Institute of Atmospheric Physics, Chinese Academy of Sciences, Beijing 100029, China. [2]Department of Earth Sciences and Planetary Sciences, University of California Riverside, Riverside, CA 92521, USA. [3]University of Chinese Academy of Sciences, Beijing 100049, China. [4]Laboratory for Regional Oceanography and Numerical Modeling, Qingdao National Laboratory for Marine Science and Technology, Qingdao 266237, China. [5]International Center for Climate and Environment Sciences, Institute of Atmospheric Physics, Chinese Academy of Sciences, Beijing 10029, China.
*Corresponding author. Email: hg@mail.iap.ac.cn

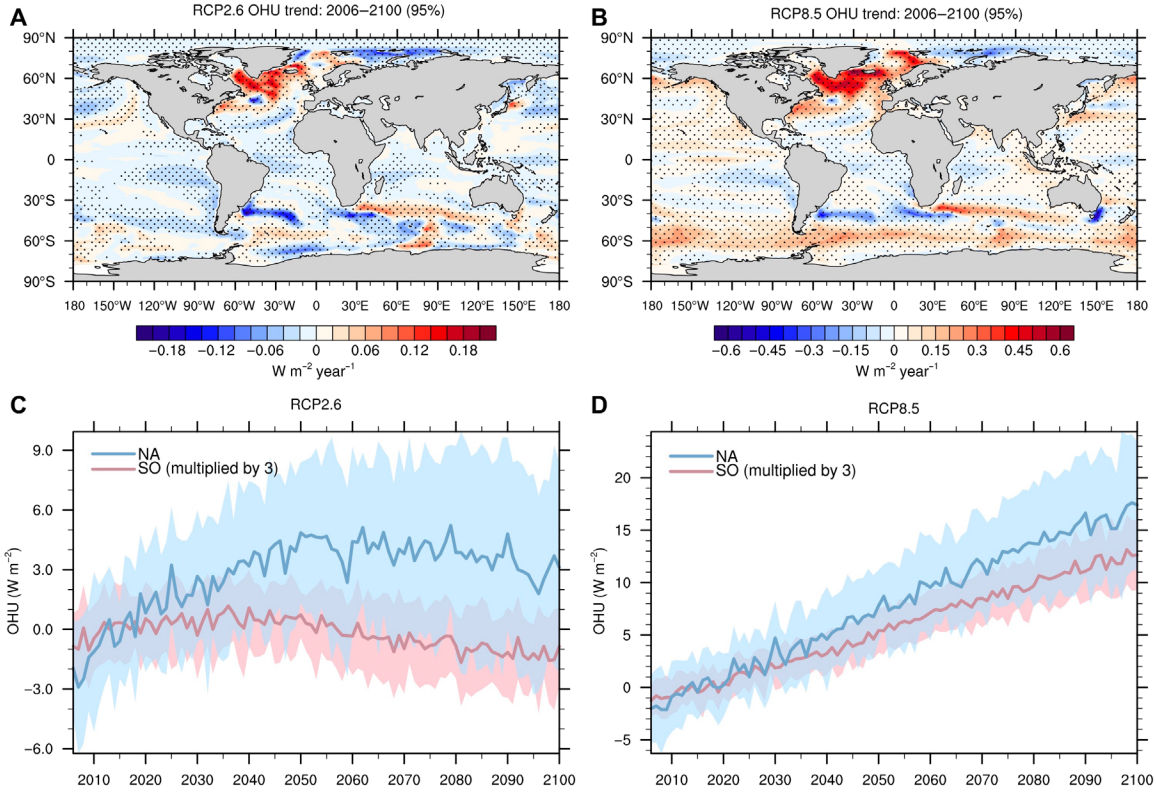

Fig. 1. CMIP5-simulated OHU changes under the RCP2.6 and RCP8.5 scenarios. Top row: CMIP5 MME OHU trends during 2006–2100 under the (**A**) RCP2.6 and (**B**) RCP8.5 scenarios. Stippling denotes where the OHU trends are statistically significant at the 95% confidence level based on the Student's *t* test. Positive (negative) values mean ocean gains (losses) heat. Bottom row: Annual mean OHU anomalies of CMIP5 model averaged over the North Atlantic (35°N to 70°N, 80°W to 10°W; MME, blue curve; model spread, blue shading) and averaged over the Southern Ocean (35°S to 70°S, 0° to 360°; MME, pink curve; model spread, pink shading) during 2006–2100 under the (**C**) RCP2.6 and (**D**) RCP8.5 scenarios. Anomalies are relative to the 2006–2025 mean. Model spread is represented by 1 SD of model results. Southern Ocean OHU anomalies are multiplied by a factor of 3 for a better illustration.

than the decline of CO_2 as projected under the RCP2.6 scenario, which might be associated with the stratospheric ozone recovery since the 2000s (*28*). In contrast, under the RCP8.5 scenario, OHU in both basins shows significant positive trends during 2006–2100, with the stronger one in the North Atlantic (Fig. 1B). For both basins, the regionally averaged OHU increases rapidly throughout the current century, with a larger trend in the North Atlantic (0.209 W m^{-2} year^{-1}, $P < 0.01$) relative to the Southern Ocean (0.154 W m^{-2} year^{-1}, $P < 0.01$) (Fig. 1D). Here, it merits attention that time series of regionally averaged OHU are not strictly linear in both the North Atlantic and Southern Ocean under both the RCP2.6 and RCP8.5 scenarios, which are largely due to complex trajectories of aerosols and GHGs. To explore the scenario-driven uncertainty in regional OHU, we resort to a common metric—the OHU trend during 2006–2100—to compare the primary regional OHU changes on a centurial time scale between the two scenarios. To summarize, the CMIP5 MME results suggest that regional OHU projections vary substantially between the mitigation and business-as-usual scenarios, which is potentially owing to the different trajectories of anthropogenic aerosols and GHGs between the two scenarios.

In addition, we investigate the relationship between aerosol radiative effect and regional OHU in CMIP5 models. In each model, the total aerosol radiative effect is estimated as aerosol effective radiative forcing (ERF) (Materials and Methods). We demonstrate the relationship between aerosol ERF and regional OHU trend during the 21st century among 15 of the 26 CMIP5 models according to the availability of model aerosol ERF (table S1) (*6*). Over the Southern Ocean, the correlation between aerosol ERF and OHU trend is not significant under both scenarios (Fig. 2, C and D), indicative of a potentially small influence of aerosols on the Southern Ocean OHU, while in the North Atlantic, a significant positive correlation between aerosol ERF and OHU trend is evident under either the RCP2.6 or the RCP8.5 scenario (Fig. 2, A and B), which means that models with stronger aerosol ERFs generally simulate larger centurial OHU trends in the North Atlantic. In addition, the correlation coefficient is larger under the RCP2.6 scenario than that under the RCP8.5 scenario. Under the RCP2.6 scenario, models with no aerosol indirect effects (Materials and Methods) show the smallest OHU trends, while models with both aerosol indirect effects (Materials and Methods) show the largest OHU trends (Fig. 2A). As such, our result confirms the importance of aerosol effects on the North Atlantic OHU, especially for the RCP2.6 scenario, although it might be partially affected by the implicit tuning of models over the historical period due to uncertainty in aerosol ERF and climate sensitivity (*29*, *30*).

Roles of anthropogenic aerosols and GHGs in modulating regional OHU

To further explore the roles of anthropogenic aerosols and GHGs in modulating regional OHU under the RCP2.6 and RCP8.5 scenarios, we choose a broadly used CMIP5 model—the Community Earth

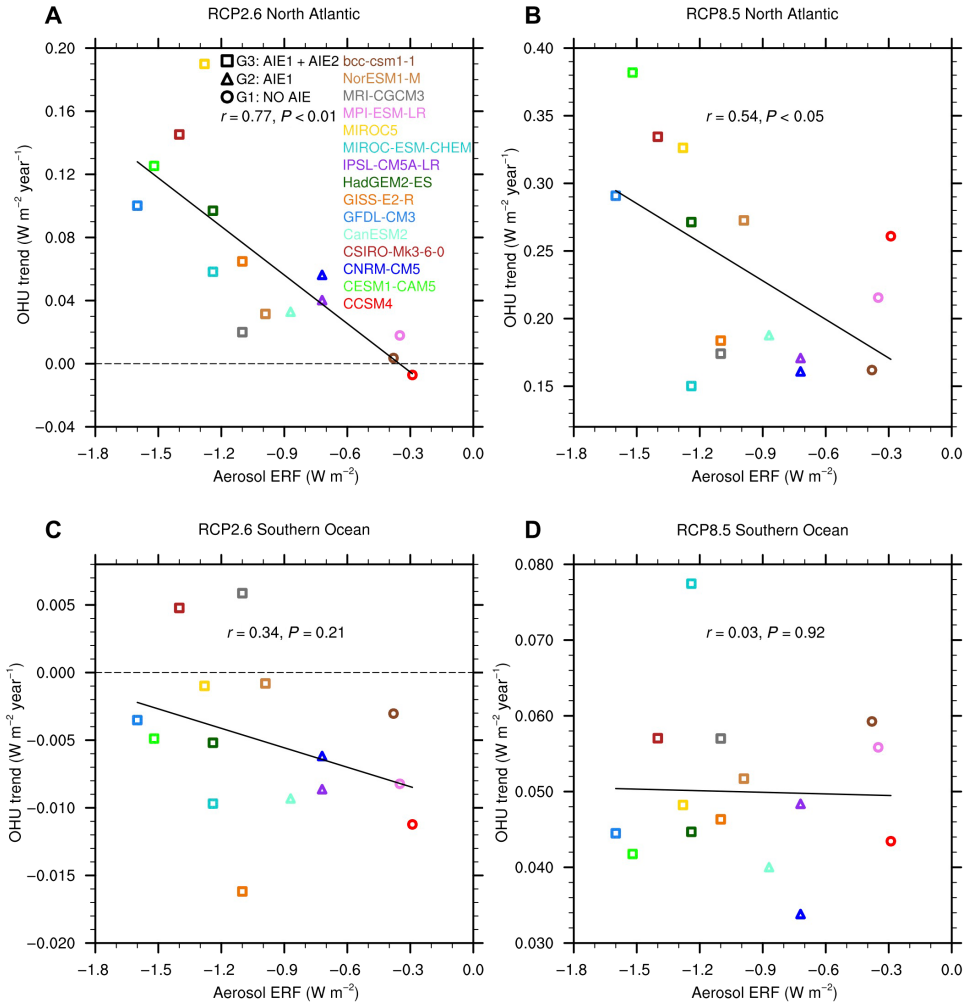

Fig. 2. Relationships between aerosol ERFs and regional OHU trends in CMIP5 models over the 21st century under the RCP2.6 and RCP8.5 scenarios. Top row: Aerosol ERFs of 2000 relative to 1850 and North Atlantic OHU trends of 2006–2100 under the (**A**) RCP2.6 and (**B**) RCP8.5 scenarios in CMIP5 models. Bottom row: As in the top row but for aerosol ERFs and Southern Ocean OHU trends (**C** and **D**). Models are denoted by different colors. Models with no aerosol indirect effects (G1: NO AIE) are denoted by circles. Models with only the first aerosol indirect effects, cloud albedo effects (G2: AIE1), are denoted by triangles. Models with both aerosol indirect effects, cloud albedo and cloud lifetime effects (G3: AIE1 + AIE2), are denoted by squares. Solid black line in each panel represents the linear regression line for the scatters. Correlation coefficient (*r*) between ERFs and OHU trends and *P* value are noted in each case. Notice the different scales in each panel.

System Model version 1 with the Community Atmosphere Model version 5 (CESM1-CAM5; Materials and Methods). CESM1-CAM5 includes both aerosol indirect effects and shows an aerosol ERF of −1.52 W m^{-2} in 2000 relative to 1850, which is strong (table S1) but still within the range of uncertainty estimates of CMIP5 models (for CMIP5 models, 90% confidence level of aerosol ERF corresponds to −2.0 to −0.4 W m^{-2}) (*31*). Given the importance of aerosols to North Atlantic OHU, CESM1-CAM5 projects a large OHU change in the North Atlantic at least partially due to its strong aerosol ERF (Fig. 2, A and B). Nevertheless, this model does well capture the characteristics of centennial OHU evolution patterns as in CMIP5 MME for both North Atlantic and Southern Ocean under both the RCP2.6 and RCP8.5 scenarios. Using CESM1-CAM5, we conduct parallel sensitivity experiments with fixed present-day anthropogenic aerosol emissions (rcpFA26 and rcpFA85 hereafter; Materials and Methods) based on the archived all-forcing CESM1-CAM5 simulations for the RCP2.6 and RCP8.5 scenarios (rcp26 and rcp85 hereafter; Materials and Methods). The difference between the two experiments in each pair (rcp26-rcpFA26 or rcp85-rcpFA85) then yields the net climate effect of future anthropogenic aerosols reduction under each scenario.

We find that major differences of regional OHU changes between rcp26 and rcpFA26 occur in the North Atlantic. OHU exhibits a much stronger positive centurial trend in the subpolar North Atlantic in rcp26 than that in rcpFA26 (Fig. 3, A and C). The regionally averaged OHU time series show that North Atlantic OHU in rcp26 increases throughout the century (0.126 W m^{-2} $year^{-1}$, $P < 0.01$) with a larger rate before 2050 (0.243 W m^{-2} $year^{-1}$, $P < 0.01$), while North Atlantic OHU in rcpFA26 increases before the 2040s and then declines until 2100 (Fig. 4A). On the other hand, OHU changes in the Southern Ocean are highly similar between the two simulations. In both rcp26 and rcpFA26, Southern Ocean OHU exhibits generally negative centurial trends during 2006–2100 (Fig. 3, A and C). The regionally averaged OHU time series depict that Southern Ocean OHU peaks around the 2030s and diminishes afterward (Fig. 4C).

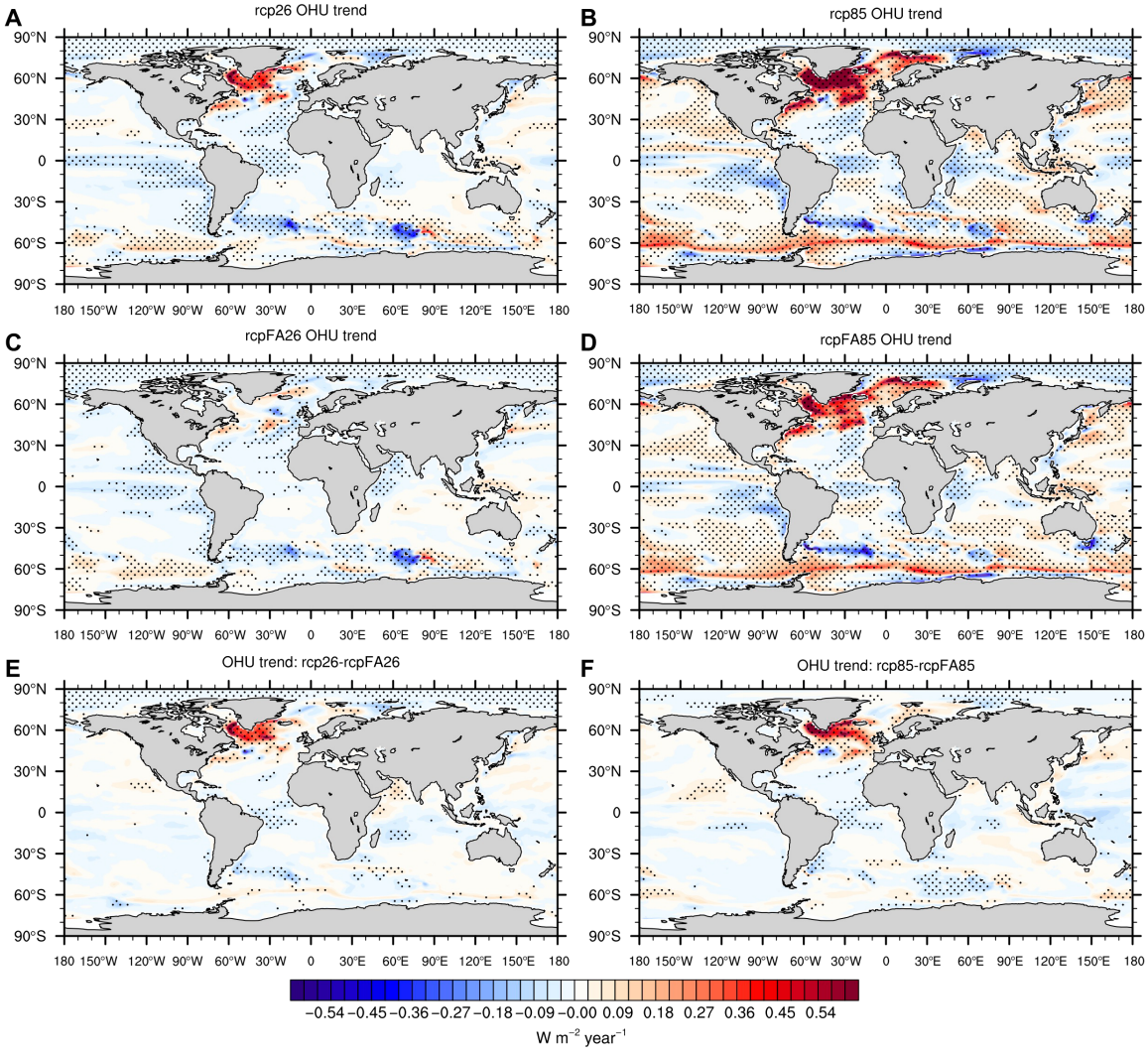

Fig. 3. CESM1-CAM5 OHU trends under the RCP2.6 and RCP8.5 scenarios and aerosol effects on OHU trends. Left column: OHU trends during 2006–2100 (**A**) in rcp26 and (**C**) rcpFA26 simulations with CESM1-CAM5 and (**E**) for their difference (rcp26-rcpFA26), which indicates aerosol effects. Right column: As in the left column but for (**B**) rcp85 and (**D**) rcpFA85 and (**F**) their difference. Stippling denotes where trends are statistically significant at the 95% confidence level based on the Student's *t* test. Positive (negative) values mean ocean gains (losses) heat.

The comparison between rcp26 and rcpFA26 suggests that the interhemispheric contrast of future OHU change is evident only when aerosol effects are included. This is because anthropogenic aerosols mainly concentrate in the Northern Hemisphere and are projected to decline under the RCP2.6 scenario (figs. S1 and S2; see Supplementary Materials), which produces an extra warming effect superimposed on the GHG effect. In the North Atlantic, OHU response is primarily attributed to the total effects of anthropogenic aerosols and GHGs. In rcp26, North Atlantic OHU increases at a larger rate before 2050 and then continues to increase until 2100 (Fig. 4A). This is consistent with the extra aerosol warming effect under the RCP2.6 scenario, as reflected by the aerosol evolution of large decrease before 2050 and continued reduction until 2100 (fig. S2). However, in rcpFA26, North Atlantic OHU decreases after 2050 (Fig. 4A), following the GHG evolution under the RCP2.6 scenario. Differences of North Atlantic OHU between rcp26 and rcpFA26 can be seen from the significant positive long-term trend during 2006–2100 within the subpolar North Atlantic in rcp26-rcpFA26 (Fig. 3E). Over the Southern Ocean, the OHU difference between rcp26 and rcpFA26 is not robust (Figs. 3E and 4C) primarily due to a minimal effect of anthropogenic aerosols.

We also compare rcp85 and rcpFA85 and find that the significant OHU differences due to aerosol effects again occur in the subpolar North Atlantic (Fig. 3F). As anthropogenic aerosols decline under the RCP8.5 scenario (fig. S2), North Atlantic OHU in rcpFA85 shows a smaller positive trend than that in rcp85 (Fig. 3, B and D), largely owing to the lack of aerosol-induced warming. Meanwhile, this difference can be seen from regional averaged OHU time series in which North Atlantic OHU increases at a smaller rate in rcpFA85 (0.241 W m^{-2} $year^{-1}$, $P < 0.01$) than rcp85 (0.379 W m^{-2} $year^{-1}$, $P < 0.01$) during 2006–2100 (Fig. 4B). Over the Southern Ocean, anthropogenic aerosol effects are minimal, while GHG effects are major. Southern Ocean OHU exhibits highly similar evolution patterns in both rcpFA85 and rcp85, featuring continuous increases during

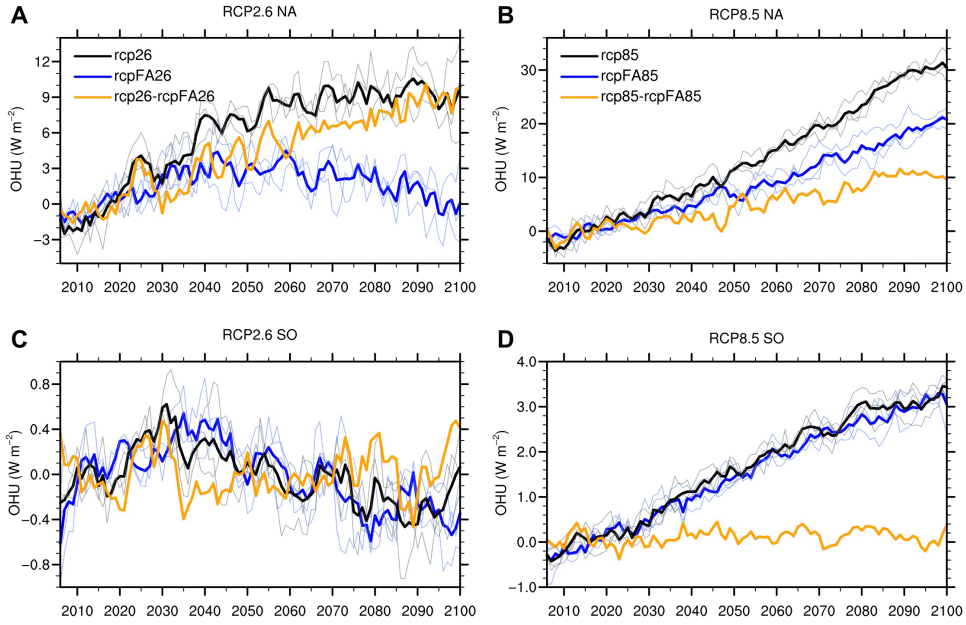

Fig. 4. CESM1-CAM5 regional OHU time series under the RCP2.6 and RCP8.5 scenarios. Top row: Annual mean OHU anomalies averaged over the North Atlantic (NA) (35°N to 70°N, 80°W to 10°W) during 2006–2100 under the (**A**) RCP2.6 and (**B**) RCP8.5 scenarios. Bottom row: As in the top row but for annual mean OHU anomalies averaged over the Southern Ocean (SO) (35°S to 70°S, 0° to 360°) (**C** and **D**). Thick black and blue curves indicate OHU anomalies in rcp and rcpFA simulations with CESM1-CAM5, which are calculated from the ensemble means of individual simulations. Thin black and blue curves denote OHU anomalies for three ensemble members in each of the rcp and rcpFA simulations. Orange lines denote the difference between the ensemble means of rcp and rcpFA simulations, which indicate aerosol effects. OHU anomalies are relative to the 2006–2025 mean and a 5-year running mean is applied. Notice the different scales in each panel.

2006–2100 (Fig. 4D; 0.041 and 0.042 W m^{-2} year^{-1}, respectively, both $P < 0.01$). To summarize, our results from CESM1-CAM5 experiments suggest that aerosol effects play an important role in the North Atlantic in future OHU changes under both the RCP2.6 and RCP8.5 scenarios. Projected decline of anthropogenic aerosols enhances OHU in the subpolar North Atlantic, resulting in positive long-term trends during 2006–2100 under both scenarios. Over the Southern Ocean, the effect of aerosols is minimal, while the effect of GHGs is major such that the projected OHU shows negative and positive long-term trends during 2006–2100 under the RCP2.6 and RCP8.5 scenarios, respectively.

Effect of aerosols on ocean heat storage via altering ocean circulation

We discover that the effect of aerosols not only acts on the OHU at Atlantic Ocean surface but also extends deep into the interior ocean and affects ocean heat storage (OHS) through altering ocean circulation and heat transport across the basin. Since 2006, the reduced anthropogenic aerosols trigger a weakened AMOC under both the RCP2.6 and RCP8.5 scenarios (fig. S3), which likely follows the mechanism as described in (*13*). Although the anthropogenic aerosol forcing turns steady after 2050 under the RCP2.6 scenario (fig. S2), the weakening of the AMOC continues, primarily owing to the subsequent ocean adjustments in the interior Atlantic Ocean (*32*). Here, we examine the difference between rcp26 and rcpFA26 simulations during three subperiods: 2006–2050, 2051–2075, and 2076–2100. When comparing the two post-2050 periods (2051–2075 and 2076–2100), we find that the continued AMOC slowdown induces a further cooling of sea surface temperatures (SSTs) in the subpolar North Atlantic (figs. S4B and S5, E and I). The enhanced SST cooling causes a further increase of North Atlantic OHU (Fig. 4A and fig. S4B) primarily via a turbulent heat flux feedback (*33*, *34*) and, meanwhile, a further reduction of evaporation to the south of Greenland (fig. S6, E and H). As a dominant factor, the intensified reduction of evaporation enlarges the surface freshwater input (fig. S6, D and G), acting to freshen the surface water to the south of Greenland. Although either surface cooling (fig. S5, E and I) or freshening (fig. S5, F and J) is present in this deep convection region, the haline effect dominates, which leads to a reduction of local sea surface density (fig. S5, G and K), a suppression of deep convection (fig. S5, H and L), and hence a further weakening of the AMOC (fig. S4B). As this loop continues, SST cooling and OHU increase persist in the subpolar North Atlantic after 2050. Under the RCP8.5 scenario, similar processes also operate (figs. S4, S7, and S8).

We further conduct an ocean heat budget analysis on the Atlantic (*18*, *20*, *21*, *35*, *36*) during 2006–2100 for either scenario using CESM1-CAM5 simulations, which incorporates OHU, OHS, meridional ocean heat transport (OHT), and diffusive processes into a dynamically consistent framework (Materials and Methods). From the difference of the 2006–2100 averages of rcp26 and rcpFA26, we find that the aerosol-driven AMOC change shows the maximum weakening at ~40°N, around the latitude of climatological AMOC maximum under the RCP2.6 scenario (Fig. 5E and fig. S3). This AMOC decline brings about a reduced northward OHT across the Atlantic primarily through its Eulerian-mean component (Fig. 5G). The magnitude of OHT reduction markedly diminishes poleward from ~40°N, leading to a meridional divergence of OHT in the subpolar North Atlantic (Fig. 5I). The OHT divergence acts to cool the whole column ocean waters in the subpolar North Atlantic (fig. S9A), which triggers more heat uptake from the atmosphere via ocean surface (Fig. 5, A and I) to

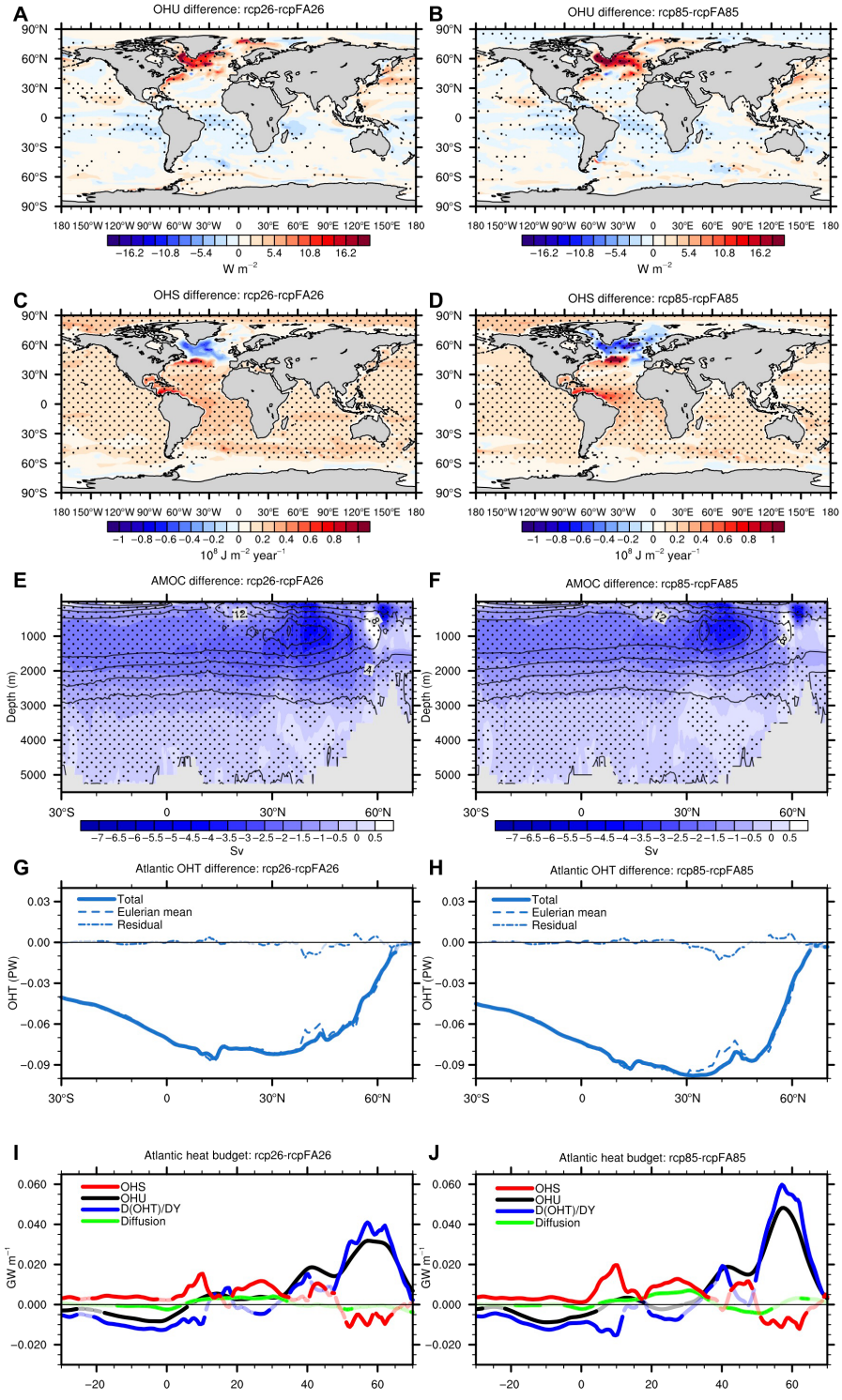

Fig. 5. CESM1-CAM5 aerosol effects on OHU and ocean heat redistribution under the RCP2.6 (left) and RCP8.5 (right) scenarios. Left column: Differences of annual mean (**A**) OHU (positive into the ocean); (**C**) OHS (positive values mean increases of heat in the ocean); (**E**) meridional overturning streamfunction in the Atlantic (negative values denote the weakening of meridional circulation); (**G**) OHT in the Atlantic (positive values denote anomalous northward heat transport): heat transport induced by total advection (solid), Eulerian-mean advection (dashed), and their residual (dotted; including eddy-induced advection and sub-mesoscale advection); (**I**) heat budget in the Atlantic: zonally integrated full-depth OHS (red), zonally integrated OHU (black), divergence of OHT induced by advections (blue), and zonally integrated full-depth heat change due to diffusive processes (green) during 2006–2100 under the RCP2.6 scenario. Right column: As in the left column but for the RCP8.5 scenario (**B**, **D**, **F**, **H**, and **J**). Stippling in the top six panels denotes where differences are statistically significant at the 95% confidence level based on the Student's *t* test. In the bottom four panels, dark colors (relative to light colors) denote where differences are statistically significant at the 95% confidence level based on the Student's *t* test. Contours in (E) and (F) denote the annual mean AMOC averaged over 2006–2100 under the RCP2.6 and RCP8.5 scenarios, respectively. Curves in (I) and (J) are derived after a 7.5° running mean.

compensate for this dynamically induced cooling (*37*). Nevertheless, the compensation from enhanced OHU is incomplete, and meanwhile, a small amount of heat can escape from the subpolar region through diffusive processes. As a result, the storage of oceanic heat diminishes in the subpolar North Atlantic (Fig. 5, C and I). Here, note that in the subpolar North Atlantic, the diminished OHS represents a cooling tendency of full-depth ocean waters (fig. S9A) as consistent with the anomalous cooling of SSTs (fig. S10E).

Under the RCP8.5 scenario, the aerosol effect is similar to that under the RCP2.6 scenario. Enhanced OHU is evident over the subpolar North Atlantic (Fig. 5, B and J). The reduction of anthropogenic aerosols induces a weaker and shallower AMOC (Fig. 5F and fig. S3) and results in a redistribution of oceanic heat within the Atlantic. In particular, heat is moved from high-latitude ocean to low-latitude ocean such that OHS decreases in the former region but increases in the latter (Fig. 5D). The significantly decreased OHS in the subpolar North Atlantic is tied to the strong cooling of local full-depth ocean waters (fig. S9B), which is consistent with the cooling of local SSTs (fig. S10F).

DISCUSSION

Our study suggests that during the 21st century, the projected OHU shows respectively positive and negative trends in the North Atlantic and Southern Ocean under the RCP2.6 scenario but collectively positive trends within the two basins under the RCP8.5 scenario. Such large scenario-driven uncertainty in regional OHU projections is tightly related to different evolution patterns of anthropogenic aerosols and GHGs under both scenarios. In the RCP2.6 scenario, anthropogenic aerosol reduction potentially serves as a main factor contributing to the enhanced OHU in the North Atlantic, which is evident from the significant positive correlation between aerosol ERF and OHU trend among CMIP5 models. Over the Southern Ocean, the decreased OHU after the 2030s could be related to the projected GHG decline in the latter half of the century and stratospheric ozone recovery since the 2000s. In the RCP8.5 scenario, both anthropogenic aerosol reduction and GHG increase contribute to the OHU increase in the North Atlantic. Over the Southern Ocean, the rising GHGs promote the OHU increase throughout the 21st century given that the strong GHG effect in this scenario likely overwhelms the effect of ozone recovery. Under both the RCP2.6 and RCP8.5 scenarios, aerosol effects induce an enhanced OHU but diminished storage of oceanic heat in the subpolar North Atlantic. This is due to an aerosol-induced AMOC slowdown, which engenders a redistribution of oceanic heat from high latitudes to low latitudes.

Besides aerosol changes, other forcings such as GHG changes can also induce hemispheric contrast of SSTs and hence OHU. One example is the SST warming minimum or the so-called North Atlantic warming hole (*38*) developed to the south of Greenland under increasing CO_2 (*3*, *39*), which is suggested to be associated with an AMOC slowdown. A similar feature can be found under the RCP8.5 scenario when GHG forcing is exclusively considered (fig. S10D). This GHG-driven warming minimum, however, exhibits a smaller magnitude than that in the full SST response to the total RCP8.5 forcing. This is because the strong SST cooling driven by future anthropogenic aerosol reduction reinforces the warming minimum to the south of Greenland, making the warming hole more evident in the full SST response (fig. S10). Moreover, beyond the RCPs used in CMIP5, multiple shared socioeconomic pathway scenarios have been introduced to current CMIP6 models, which span much broader aerosol emission pathways (*40*). Improved understanding of how anthropogenic emissions affect OHU and ocean circulations under different scenarios is necessary to reduce the uncertainty of climate projections.

MATERIALS AND METHODS

Datasets

Model results from the CMIP5 of the Intergovernmental Panel on Climate Change (*41*) are used to examine OHU trends and its evolution in the North Atlantic and Southern Ocean over 2006–2100 (Fig. 1). Here, based on the availability of surface heat fluxes (SHFs) over 2006–2100, we use 26 CMIP5 models, in which 62 members of CMIP5 RCP2.6 simulation and 66 members of CMIP5 RCP8.5 simulation are analyzed (table S1). CO_2 concentrations in the RCP2.6 and RCP8.5 scenarios (*42*, *43*) are available from the RCP database website (http://tntcat.iiasa.ac.at:8787/RcpDb/dsd?Action=htmlpage&page=about).

Analysis methods

The CMIP5 MME provides an estimate of climate response to external forcing, as internal climate variability is averaged out. For each scenario, we first calculate the ensemble member mean for each model and then average the mean values from all the models to achieve the MME of CMIP5 models. This approach allows equal weighting for each model in the calculation of MME.

The least-square linear regression is used at each grid box to estimate the long-term trends over 2006–2100 for future scenarios. Long-term trends of the difference between "rcp" and "rcpFA" simulations for OHU (Fig. 3), aerosol optical depth (fig. S1), zonal-mean Atlantic Ocean temperature (fig. S9), and SSTs (fig. S10) are calculated to reveal the net anthropogenic aerosol effect. The statistical significance of trends is performed with the Student's *t* test. In Fig. 5, we take the difference between the 2006–2100 means in rcp and rcpFA simulations at each grid box to obtain the net anthropogenic aerosol effect and then calculate the significance for the difference based on the Student's *t* test.

Aerosol radiative effects

Aerosol radiative effects on climate include direct effects in which aerosols scatter and absorb shortwave radiation and indirect effects in which aerosols alter the cloud albedo (first) and cloud lifetime (second). The model representations of aerosol effects are used to further subdivide the CMIP5 models into three groups: those without aerosol indirect effects (NO AIE), those with only the first aerosol indirect effect (AIE1), and those with both aerosol indirect effects (AIE1 + AIE2) (table S1). For climate models, ERF is calculated from the top-of-the-atmosphere (TOA) flux differences between atmosphere-only simulations with identical SSTs but different atmospheric compositions (*44*), and aerosol ERF is calculated as the TOA flux difference between the atmosphere-only simulation with aerosol forcing and that without aerosol forcing. Models that include aerosol indirect effects generally have larger aerosol ERF than models that do not include aerosol indirect effects, and models with both aerosol indirect effects generally have larger aerosol ERF than those with only one aerosol indirect effect (Fig. 2).

The NCAR CESM1-CAM5 and the fixed-aerosol experiments

The CESM1-CAM5 coupled climate model (*45*) from the National Center for Atmospheric Research (NCAR) is used to investigate the

responses of OHU and ocean heat redistribution to the projected decline of anthropogenic aerosols under the RCP2.6 and RCP8.5 scenarios. The atmosphere component is the CAM5. The ocean component is the Parallel Ocean Program version 2. The land component is the Community Land Model version 4. The sea ice component is the Community Ice Code version 4. We use the f09_g16 version, with ~1° horizontal resolution and 30 vertical levels in the atmosphere component and ~1° horizontal resolution and 60 vertical levels in the ocean component. In CESM1-CAM5, the total surface freshwater flux into the ocean is computed as a sum of precipitation (P) minus evaporation ($-E$), river runoff (R), freshwater fluxes due to sea ice melting (M), and brine rejection (Br) and other sources.

We use the archived rcp simulations (rcp26 and rcp85) with CESM1-CAM5. Each rcp simulation is composed of three ensemble members over 2006–2100 and is available from the CMIP5 archives. Using CESM1-CAM5, we perform the rcpFA experiments (rcpFA26 and rcpFA85) from 2006 to 2100 under the same RCP scenarios except that the emissions of anthropogenic aerosols and their precursors (including aerosols from biomass burning) are fixed at 2005 levels with a constant annual cycle. All the other forcings are identical as in rcp simulations. For both rcpFA26 and rcpFA85 simulations, we conduct three-member ensemble simulations. Each member starts from 2006 with the initial condition obtained from the archived CESM historical simulations. Unless otherwise specified, the results of CESM simulations presented in this study are based on the three-member ensemble means of individual simulations. In model simulations, the AMOC index is defined as the maximum of streamfunction below 500 m in the Atlantic.

Ocean heat budget analysis

OHU is defined as net downward SHF into the ocean, which is equal to the sum of net surface shortwave radiation flux, net surface longwave radiation flux, latent heat flux, sensible heat flux, and fluxes from other sources. OHS is defined as the tendency of ocean heat content (OHC) and denotes the rate of oceanic heat change for full-depth water column. OHT is defined as the transport of heat by advective processes, including Eulerian-mean, eddy-induced, and sub-mesoscale advective processes.

Along each latitude of the Atlantic, the full-depth ocean heat budget follows

$$\frac{\partial}{\partial t}\int_{X_W}^{X_E}\int_{-H}^{0}\rho_0 c_p\theta dz\,dx = \int_{X_W}^{X_E}(\mathrm{SHF})\,dx - \int_{X_W}^{X_E}\int_{-H}^{0}\rho_0 c_p\ \nabla\cdot(\mathbf{v}\theta)\,dz\,dx + \int_{X_W}^{X_E}\int_{-H}^{0}\rho_0 c_p D\,dz\,dx \quad (1)$$

$\rho_0 = 1026\ \mathrm{kg\ m^{-3}}$ is seawater density, $c_p = 3996\ \mathrm{J\ K^{-1}\ kg^{-1}}$ is the specific heat capacity of seawater, θ is the potential temperature of seawater, H is the depth of ocean bottom, and X_W and X_E denote the longitudes of the western and eastern boundaries of the Atlantic, respectively. ∇ denotes the three-dimensional gradient operator and $\mathbf{v} = \overline{\mathbf{v}} + \mathbf{v}^*$, where $\overline{\mathbf{v}}$ is Eulerian-mean velocity and $\mathbf{v}^*$ denotes the sum of eddy-induced and sub-mesoscale velocities. D denotes diffusive processes.

We then define OHS as

$$\mathrm{OHS} = \frac{\partial}{\partial t}\mathrm{OHC} = \frac{\partial}{\partial t}\int_{X_W}^{X_E}\int_{-H}^{0}\rho_0 c_p\theta\,dz\,dx \quad (2)$$

OHU as

$$\mathrm{OHU} = \int_{X_W}^{X_E}(\mathrm{SHF})\,dx \quad (3)$$

OHT as

$$\mathrm{OHT} = \int_{X_W}^{X_E}\int_{-H}^{0}\rho_0 c_p(\overline{\nabla}\theta + \mathrm{v}^*\theta)\,dz\,dx = \overline{\mathrm{OHT}} + \mathrm{OHT}^* \quad (4)$$

and integrated heat change due to diffusive processes as

$$\mathrm{Diff} = \int_{X_W}^{X_E}\int_{-H}^{0}\rho_0 c_p D\,dz\,dx \quad (5)$$

where $\overline{\mathrm{OHT}} = \int_{X_W}^{X_E}\int_{-H}^{0}\rho_0 c_p\overline{\nabla}\theta dz\,dx$ denotes the OHT by Eulerian-mean advection ($\overline{\nabla}$ is Eulerian-mean meridional velocity) and $\mathrm{OHT}^* = \int_{X_W}^{X_E}\int_{-H}^{0}\rho_0 c_p\mathrm{v}^*\theta dz\,dx$ denotes the OHT by eddy-induced and sub-mesoscale advection (v^* is the sum of eddy-induced and sub-mesoscale meridional velocities). Hence, the heat budget (Eq. 1) can be written as

$$\mathrm{OHS} = \mathrm{OHU} - \frac{\partial}{\partial y}\mathrm{OHT} + \mathrm{Diff} \quad (6)$$

As can be seen from Eq. 6, OHS is determined by OHU, meridional gradient (divergence) of OHT, and heat change due to diffusive processes.

SUPPLEMENTARY MATERIALS

Supplementary material for this article is available at http://advances.sciencemag.org/cgi/content/full/6/45/eabc0303/DC1

REFERENCES AND NOTES

1. K. von Schuckmann, M. D. Palmer, K. E. Trenberth, A. Cazenave, D. Chambers, N. Champollion, J. Hansen, S. A. Josey, N. Loeb, P.-P. Mathieu, B. Meyssignac, M. Wild, An imperative to monitor Earth's energy imbalance. *Nat. Clim. Change* **6**, 138–144 (2016).
2. J. M. Gregory, J. A. Church, G. J. Boer, K. W. Dixon, G. M. Flato, D. R. Jackett, J. A. Lowe, S. P. O'Farrell, E. Roeckner, G. L. Russell, R. J. Stouffer, M. Winton, Comparison of results from several AOGCMs for global and regional sea-level change 1900–2100. *Clim. Dynam.* **18**, 225–240 (2001).
3. M. Winton, K. Takahashi, I. M. Held, Importance of ocean heat uptake efficacy to transient climate change. *J. Climate* **23**, 2333–2344 (2010).
4. B. E. J. Rose, K. C. Armour, D. S. Battisti, N. Feldl, D. D. B. Koll, The dependence of transient climate sensitivity and radiative feedbacks on the spatial pattern of ocean heat uptake. *Geophys. Res. Lett.* **41**, 1071–1078 (2014).
5. S. M. Kang, I. M. Held, D. M. W. Frierson, M. Zhao, The response of the ITCZ to extratropical thermal forcing: Idealized slab-ocean experiments with a GCM. *J. Climate* **21**, 3521–3532 (2008).
6. R. J. Allen, O. Ajoku, Future aerosol reductions and widening of the northern tropical belt. *J. Geophys. Res. Atmos.* **121**, 6765–6786 (2016).
7. S. Levitus, J. I. Antonov, T. P. Boyer, O. K. Baranova, H. E. Garcia, R. A. Locarnini, A. V. Mishonov, J. R. Reagan, D. Seidov, E. S. Yarosh, M. M. Zweng, World ocean heat content and thermosteric sea level change (0–2000 m), 1955–2010. *Geophys. Res. Lett.* **39**, L10603 (2012).
8. D. Roemmich, J. Church, J. Gilson, D. Monselesan, P. Sutton, S. Wijffels, Unabated planetary warming and its ocean structure since 2006. *Nat. Clim. Change* **5**, 240–245 (2015).
9. T. L. Frölicher, J. L. Sarmiento, D. J. Paynter, J. P. Dunne, J. P. Krasting, M. Winton, Dominance of the southern ocean in anthropogenic carbon and heat uptake in CMIP5 models. *J. Climate* **28**, 862–886 (2015).
10. R. A. F. Bilbao, J. M. Gregory, N. Bouttes, M. D. Palmer, P. Stott, Attribution of ocean temperature change to anthropogenic and natural forcings using the temporal, vertical and geographical structure. *Clim. Dynam.* **53**, 5389–5413 (2019).
11. D. Paynter, T. L. Frölicher, Sensitivity of radiative forcing, ocean heat uptake, and climate feedback to changes in anthropogenic greenhouse gases and aerosols. *J. Geophys. Res. Atmos.* **120**, 9837–9854 (2015).

12. D. B. Irving, S. Wijffels, J. A. Church, Anthropogenic aerosols, greenhouse gases, and the uptake, transport, and storage of excess heat in the climate system. *Geophys. Res. Lett.* **46**, 4894–4903 (2019).
13. M. B. Menary, C. D. Roberts, M. D. Palmer, P. R. Halloran, L. Jackson, R. A. Wood, W. A. Müller, D. Matei, S.-K. Lee, Mechanisms of aerosol-forced AMOC variability in a state of the art climate model. *J. Geophys. Res. Oceans* **118**, 2087–2096 (2013).
14. J. M. Gregory, K. W. Dixon, R. J. Stouffer, A. J. Weaver, E. Driesschaert, M. Eby, T. Fichefet, H. Hasumi, A. Hu, J. H. Jungclaus, I. V. Kamenkovich, A. Levermann, M. Montoya, S. Murakami, S. Nawrath, A. Oka, A. P. Sokolov, R. B. Thorpe, A model intercomparison of changes in the Atlantic thermohaline circulation in response to increasing atmospheric CO_2 concentration. *Geophys. Res. Lett.* **32**, L12703 (2005).
15. A. J. Weaver, M. Eby, M. Kienast, O. A. Saenko, Response of the Atlantic meridional overturning circulation to increasing atmospheric CO_2: Sesnsitivity to mean climate state. *Geophys. Res. Lett.* **34**, L05708 (2007).
16. J. Marshall, J. R. Scott, K. C. Armour, J.-M. Campin, M. Kelley, A. Romanou, The ocean's role in the transient response of climate to abrupt greenhouse gas forcing. *Clim. Dynam.* **44**, 2287–2299 (2014).
17. M. Winton, S. M. Griffies, B. L. Samuels, J. L. Sarmiento, T. L. Frölicher, Connecting changing ocean circulation with changing climate. *J. Climate* **26**, 2268–2278 (2013).
18. C. He, Z. Liu, A. Hu, The transient response of atmospheric and oceanic heat transports to anthropogenic warming. *Nat. Clim. Change* **9**, 222–226 (2019).
19. K. C. Armour, J. Marshall, J. R. Scott, A. Donohoe, E. R. Newsom, Southern Ocean warming delayed by circumpolar upwelling and equatorward transport. *Nat. Geosci.* **9**, 549–554 (2016).
20. A. K. Morrison, S. M. Griffies, M. Winton, W. G. Anderson, J. L. Sarmiento, Mechanisms of southern ocean heat uptake and transport in a global eddying climate model. *J. Climate* **29**, 2059–2075 (2016).
21. W. Liu, J. Lu, S.-P. Xie, A. Fedorov, Southern Ocean heat uptake, redistribution, and storage in a warming climate: The role of meridional overturning circulation. *J. Climate* **31**, 4727–4743 (2018).
22. J.-R. Shi, S.-P. Xie, L. D. Talley, Evolving relative importance of the southern ocean and north atlantic in anthropogenic ocean heat uptake. *J. Climate* **31**, 7459–7479 (2018).
23. M. B. Stolpe, I. Medhaug, J. Sedláček, R. Knutti, Multidecadal variability in global surface temperatures related to the atlantic meridional overturning circulation. *J. Climate* **31**, 2889–2906 (2018).
24. O. Boucher, D. Randall, P. Artaxo, C. Bretherton, G. Feingold, P. Forster, V.-M. Kerminen, Y. Kondo, H. Liao, U. Lohmann, P. Rasch, S. K. Satheesh, S. Sherwood, B. Stevens, X. Y. Zhang, Clouds and Aerosols, in *Climate Change 2013: The Physical Science Basis. Contribution of Working Group I to the Fifth Assessment Report of the Intergovernmental Panel on Climate Change*, T. F. Stocker, D. Qin, G.-K. Plattner, M. Tignor, S. K. Allen, J. Boschung, A. Nauels, Y. Xia, V. Bex, P. M. Midgley, Eds. (Cambridge Univ. Press, 2013).
25. D. P. van Vuuren, J. Edmonds, M. Kainuma, K. Riahi, A. Thomson, K. Hibbard, G. C. Hurtt, T. Kram, V. Krey, J.-F. Lamarque, T. Masui, M. Meinshausen, N. Nakicenovic, S. J. Smith, S. K. Rose, The representative concentration pathways: An overview. *Clim. Change* **109**, 5 (2011).
26. IPCC, Summary for Policymakers, in *Global warming of 1.5°C. An IPCC Special Report on the Impacts of Global Warming of 1.5°C Above Pre-industrial Levels and Related Global Greenhouse Gas Emission Pathways, in The Context of Strengthening the Global Response to the Threat of Climate Change, Sustainable Development, and Efforts to Eradicate Poverty*, V. Masson-Delmotte, P. Zhai, H. O. Pörtner, D. Roberts, J. Skea, P. R. Shukla, A. Pirani, W. Moufouma-Okia, C. P. an, R. Pidcock, S. Connors, J. B. R. Matthews, Y. Chen, X. Zhou, M. I. Gomis, E. Lonnoy, T. Maycock, M. Tignor, T. Waterfield, Eds. (World Meteorological Organization, 2018), 32 pp.
27. S.-M. Long, S.-P. Xie, Y. Du, Q. Liu, X.-T. Zheng, G. Huang, K.-M. Hu, J. Ying, Effects of ocean slow response under low warming targets. *J. Climate* **33**, 477–496 (2020).
28. K. L. Smith, L. M. Polvani, D. R. Marsh, Mitigation of 21st century Antarctic sea ice loss by stratospheric ozone recovery. *Geophys. Res. Lett.* **39**, L20701 (2012).
29. J. T. Kiehl, Twentieth century climate model response and climate sensitivity. *Geophys. Res. Lett.* **34**, –L22710 (2007).
30. R. Knutti, Why are climate models reproducing the observed global surface warming so well? *Geophys. Res. Lett.* **35**, L18704 (2008).
31. N. Bellouin, J. Quaas, E. Gryspeerdt, S. Kinne, P. Stier, D. Watson-Parris, O. Boucher, K. S. Carslaw, M. Christensen, A.-L. Daniau, J.-L. Dufresne, G. Feingold, S. Fiedler, P. Forster, A. Gettelman, J. M. Haywood, U. Lohmann, F. Malavelle, T. Mauritsen, D. T. McCoy, G. Myhre, J. Mülmenstädt, D. Neubauer, A. Possner, M. Rugenstein, Y. Sato, M. Schulz, S. E. Schwartz, O. Sourdeval, T. Storelvmo, V. Toll, D. Winker, B. Stevens, Bounding global aerosol radiative forcing of climate change. *Rev. Geophys.* **58**, e2019RG000660 (2020).
32. M. Kawase, Establishment of deep ocean circulation driven by deep-water production. *J. Phys. Oceanogr.* **17**, 2294–2317 (1987).
33. U. Hausmann, A. Czaja, J. Marshall, Mechanisms controlling the SST air-sea heat flux feedback and its dependence on spatial scale. *Clim. Dynam.* **48**, 1297–1307 (2017).
34. W. Liu, A. V. Fedorov, Global impacts of Arctic sea ice loss mediated by the Atlantic meridional overturning circulation. *Geophys. Res. Lett.* **46**, 944–952 (2019).
35. M. A. Rugenstein, M. Winton, R. J. Stouffer, S. M. Griffies, R. Hallberg, Northern high-latitude heat budget decomposition and transient warming. *J. Climate* **26**, 609–621 (2013).
36. S. Hu, S.-P. Xie, W. Liu, Global pattern formation of net ocean surface heat flux response to greenhouse warming. *J. Climate* **33**, 7503–7522 (2020).
37. W. Liu, A. V. Fedorov, S.-P. Xie, S. Hu, Climate impacts of a weakened Atlantic Meridional Overturning Circulation in a warming climate. *Sci. Adv.* **6**, eaaz4876 (2020).
38. H. Kim, S.-I. An, On the subarctic North Atlantic cooling due to global warming. *Theor. Appl. Climatol.* **114**, 9–19 (2013).
39. C. Li, J.-S. von Storch, J. Marotzke, Deep-ocean heat uptake and equilibrium climate response. *Clim. Dynam.* **40**, 1071–1086 (2013).
40. V. Eyring, S. Bony, G. A. Meehl, C. A. Senior, B. Stevens, R. J. Stouffer, K. E. Taylor, Overview of the coupled model intercomparison project phase 6 (CMIP6) experimental design and organization. *Geosci. Model Dev.* **9**, 1937–1958 (2016).
41. K. E. Taylor, R. J. Stouffer, G. A. Meehl, An overview of CMIP5 and the experiment design. *Bull. Am. Meteorol. Soc.* **93**, 485–498 (2012).
42. D. P. van Vuuren, M. G. J. den Elzen, P. L. Lucas, B. Eickhout, B. J. Strengers, B. van Ruijven, S. Wonink, R. van Houdt, Stabilizing greenhouse gas concentrations at low levels: An assessment of reduction strategies and costs. *Clim. Change* **81**, 119–159 (2007).
43. K. Riahi, A. Grübler, N. Nakicenovic, Scenarios of long-term socio-economic and environmental development under climate stabilization. *Technol. Forecast. Soc. Change* **74**, 887–935 (2007).
44. P. M. Forster, T. Richardson, A. C. Maycock, C. J. Smith, B. H. Samset, G. Myhre, T. Andrews, R. Pincus, M. Schulz, Recommendations for diagnosing effective radiative forcing from climate models for CMIP6. *J. Geophys. Res. Atmos.* **121**, 12460–12475 (2016).
45. J. W. Hurrell, M. M. Holland, P. R. Gent, S. Ghan, J. E. Kay, P. J. Kushner, J.-F. Lamarque, W. G. Large, D. Lawrence, K. Lindsay, W. H. Lipscomb, M. C. Long, N. Mahowald, D. R. Marsh, R. B. Neale, P. Rasch, S. Vavrus, M. Vertenstein, D. Bader, W. D. Collins, J. J. Hack, J. Kiehl, S. Marshall, The community earth system model: A framework for collaborative research. *Bull. Am. Meteorol. Soc.* **94**, 1339–1360 (2013).

Acknowledgments: We thank the National Center for Atmospheric Research for providing the CESM1-CAM5 coupled general circulation model and the World Climate Research Programme's Working Group on Coupled Modelling for providing the CMIP5 multimodel datasets. **Funding:** X.M. and G.H. were supported by the National Natural Science Foundation of China (91937302, 41831175, 41676190, and 41721004), the Chinese Academy of Sciences (COMS2019Q03 and XDA20060501), the National Key R&D Program of China (2018YFA0605904). X.L. is supported by the National Natural Science Foundation of China (41676190 and 41976193). X.M. is supported by the China Scholarship Council. **Author contributions:** X.M. conceived the project, designed model experiments, performed model simulations, carried out the data analysis, and prepared all figures. R.J.A. helped to set up the model simulations. X.M. led the writing of the paper. W.L. and R.J.A. advised on interpretations of the results. All authors discussed the results and commented on the manuscript. **Competing interests:** The authors declare that they have no competing interests. **Data and materials availability:** All data needed to evaluate the conclusions in the paper are present in the paper and/or the Supplementary Materials. Additional data related to this paper may be requested from the authors. The CMIP5 data are publicly available at ESFG data portal (https://esgf-data.dkrz.de/search/esgf-dkrz/).

Submitted 7 April 2020
Accepted 21 September 2020
Published 6 November 2020
10.1126/sciadv.abc0303

Citation: X. Ma, W. Liu, R. J. Allen, G. Huang, X. Li, Dependence of regional ocean heat uptake on anthropogenic warming scenarios. *Sci. Adv.* **6**, eabc0303 (2020).